Multibeam field emission x-ray system with half-scan reconstruction algorithm

Yang Lu[a)]
Department of Biomedical Engineering, Shanghai Jiao Tong University, Shanghai 200240, China

Hengyong Yu
SBES Division and ICTAS Center for Biomedical Imaging, Virginia Tech, Blacksburg, Virginia 24061

Guohua Cao
Department of Physics and Astronomy, University of North Carolina, Chapel Hill, North Carolina 27599

Jun Zhao
Department of Biomedical Engineering, Shanghai Jiao Tong University, Shanghai 200240, China

Ge Wang
SBES Division and ICTAS Center for Biomedical Imaging, Virginia Tech, Blacksburg, Virginia 24061

Otto Zhou
Department of Physics and Astronomy, University of North Carolina, Chapel Hill, North Carolina 27599

Purpose: In this article, the authors propose a multibeam field emission x-ray (MBFEX) system along with a half-scan fan-beam reconstruction algorithm.

Methods: The proposed system consists of a linear CNT-based MBFEX source array, a single large area detector that is divided into same number of segments as the number of x-ray beams, a multihole collimator that aligns each beam with a corresponding detector segment, and a sample rotation stage. The collimator is placed between the source and the object to restrict the x-ray radiations through the target object only. In this design, all the x-ray beams are activated simultaneously to provide multiple projection views of the object. The detector is virtually segmented and synchronized with the x-ray exposure and the physiological signals when gating is involved. The transmitted x-ray intensity from each beam is collected by the corresponding segment on the detector. After each exposure, the object is rotated by a step angle until sufficient data set is collected. The half-scan reconstruction formula for MBFEX system is derived from the conventional filtered backprojection algorithm. To demonstrate the advantages of the system and method in reducing motion artifacts, the authors performed simulations with both standard and dynamic Shepp–Logan phantoms.

Results: The numerical results indicate that the proposed multibeam system and the associated half-scan algorithm can effectively reduce the scanning time and improve the image quality for a time-varying object.

Conclusions: The MBFEX technique offers an opportunity for the innovation of multisource imaging system. © *2010 American Association of Physicists in Medicine*. [DOI: 10.1118/1.3446801]

Key words: multibeam field emission x-ray system (MBFEX), half-scan algorithm, image reconstruction

I. INTRODUCTION

Microcomputed tomography (micro-CT) has recently emerged as a powerful noninvasive imaging tool for biomedical imaging of small animals, which has increasingly played a critical role in phenotyping, drug discovery, and in providing a basic understanding of mechanisms of disease. However, motion-induced artifacts blur the micro-CT image and result in deteriorated spatial resolution than the nominal values. The physiological motions of a mouse are about ten times faster than humans. To minimize the motion blurs, at least ten times faster temporal resolution than that of humans is necessary. This poses a particular challenge for micro-CT system design because it requires not only short exposure (hence high temporal resolution) and high fluency rate, but also small focal spot size to achieve high system resolution without compromising the imaging quality.[1]

To address the abovementioned conflicting requirements for both high spatial and temporal resolution, Dr. Otto Zhou's group at the University of North Carolina at Chapel Hill recently developed a dynamic micro-CT scanner based on a carbon nanotube (CNT) field emission microfocus x-ray source that can potentially deliver spatial resolution better than 100 μm and 50 ms temporal resolution.[2] Compared to the conventional thermionic microfocus x-ray sources, a primary advantage of the field emission x-ray source is its electronic programmability and the easiness for gating, even for fast nonperiodic physiological signals, including respiratory

and cardiac motions. Very recently, the performance of this scanner has been improved to 80 μm spatial resolution and 15 ms temporal resolution.[3] The key idea is that with programmability of the field emission x-ray source, the motion-induced artifacts can be minimized by prospective gating even for free-breathing mice, i.e., the image acquisition is synchronized with the animal's physiological motions. With prospective gating, however, the micro-CT scanning time becomes much longer. To acquire a single 3D data set, prospective and respiratory gated micro-CT normally takes about 10 min. In a recent study with cine cardiac micro-CT, in which as many as ten data sets were acquired of the same mouse corresponding to ten phases in a cardiac cycle, the total scanning time was as long as a few hours.[4] With such long scanning time, the imaged animal is under more stress and becomes more difficult to handle, which in turn worsens the reproducibility of gating, and therefore compromises the image quality.

The long scanning time with prospectively gated micro-CT can be greatly reduced using the multisource configuration. In history, the dynamic spatial reconstructor[5] used 14 x-ray tubes mounted on a gantry around a patient. Although high temporal resolution was demonstrated for cardiac imaging, the system is practically undesirable in terms of cost, size, and maintenance. Nowadays, most of current micro-CT systems use only a single source-detector pair and one projection is acquired within one physiological cycle. Recent technological development has led to some dual source-detector micro-CT systems (SkyScan, Model 1178, Kartuizersweg 3B, 2550 Kontich, Belgium and VAMP GmbH, TomoScope, Henkestrabe 91, 91052 Erlangen, Germany) that can reduce the scanning time by a factor of 2 because two projections can be taken simultaneously. In principle, if N projection images can be taken simultaneously, the scanning time can be reduced by a factor of N. However, we have not seen any micro-CT system with more than two conventional thermionic x-ray sources. This is partially due to the high cost associated with multiple (≥ 3) conventional thermionic x-ray sources and limited space for integration of many source-detector pairs. Interestingly, research in the past few years indicates that the CNT x-ray technology allows effective control of x-ray beams both temporally and spatially.[6] The feasibility of utilizing the CNT-based multibeam field emission x-ray (MBFEX) technology for stationary or multibeam tomography imaging systems has been demonstrated for digital breast tomosynthesis,[7] real-time tomosynthesis guidance for radiation therapy,[8] and novel computed tomography geometry.[9] Recently, a proof-of-concept multibeam micro-CT scanner operating in the sequential imaging mode has also been demonstrated.[10]

Here we propose to develop a high-speed micro-CT system using the CNT-based field emission x-ray source array. The key benefit of the proposed system is to *simultaneously* collect multiple projections, thus proportionally shortening the imaging time for prospective gated small animal imaging. In this paper, we derive a half-scan fan-beam reconstruc-
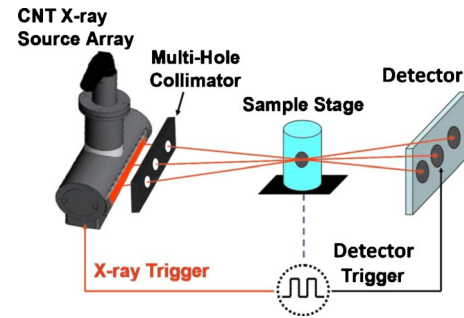

FIG. 1. The schematic of the MBFEX system.

tion formula for this new imaging geometry and evaluate the new formula with numerical simulations.

This paper is organized as follows. In Sec. II, we will discuss the configuration of the MBFEX micro-CT system, including characteristics of the MBFEX system, and the detector segmentation for different x-ray beams. In Sec. III, we will derive the formulas for projection rebinning. In Sec. IV, we will perform three numerical experiments to showcase the advantages of the proposed half-scan algorithm. In Sec. V, we will discuss the related issues and conclude the paper.

II. SYSTEM DESIGN

II.A. System development

Ideally, it is best to develop a stationary micro-CT scanner using hundreds of distributed x-ray beams and multiple detectors.[11] However, development of such a stationary scanner is limited by the practical constraints with available x-ray source and detector technology, the lack of suitable image reconstruction algorithm, and the potential issues with system geometry and scattering. Therefore, we propose to develop a micro-CT system that has a few distributed x-ray beams and requires only limited steps of rotation. As illustrated in Fig. 1, the proposed system consists of a linear CNT-based MBFEX source array, a single large area detector that is divided into the same number of segments as the number of x-ray beams, a multihole collimator that aligns each beam with a corresponding detector segment, and a sample rotation stage. The collimator is placed between the source and the object to restrict the x-ray radiations through the target object only. In this design, all the x-ray beams are activated simultaneously to provide multiple projection views of the object. The detector is virtually segmented and synchronized with the x-ray exposure and the physiological signals when gating is involved. The transmitted x-ray intensity from each beam is collected by the corresponding segment on the detector. After each exposure, the object is rotated by a step angle until sufficient data set is collected.

II.B. Detector segmentation

Unlike single source geometry, in this MBFEX system, multiple x-ray pixels share the same detector. Hence, the detector area is virtually split into several subregions corresponding to different x-ray pixels, and each of them does not
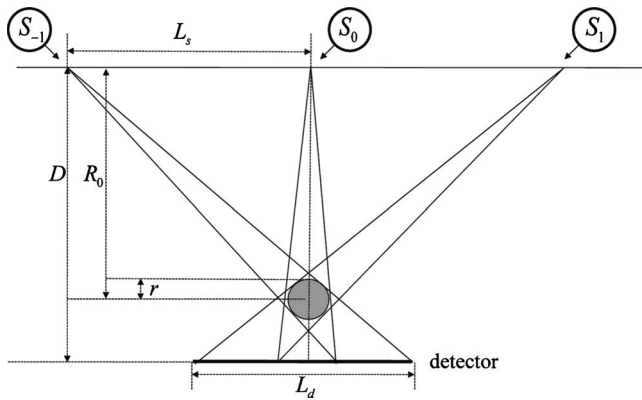
FIG. 2. The optimal design of MBFEX system with three x-ray pixels.

FIG. 3. Illustration of the data transform from the real detector to the virtual detector. (a) and (b) are for pixels S_1 (S_{-1}) and S_0, respectively.

overlap with others. Furthermore, to maximize the usage of the detector, the gaps between different subregions should be as narrow as possible. The optimal solution is illustrated as in Fig. 2. Given the detector length L_d, the distance L_s between x-ray pixels, and the radius r of ROI, the optimal solution can be achieved through changing the source-detector distance D and the source-object distance R_0. A quick calculation shows

$$R_0 = \frac{D \cdot L_s + r\sqrt{D^2 + \left(L_s + \frac{1}{2}L_d\right)^2}}{L_s + \frac{1}{2}L_d}. \tag{2.1}$$

If the number of the x-ray pixels is larger than 3, i.e., 5 or more, L_{si} and $L_{d(i+1)}$, $i=2,3\ldots$, can be calculated iteratively as (see Appendix A)

$$L_{si} = \frac{-B_1 + \sqrt{B_1^2 - 4A_1C_1}}{2A_1}, \quad L_{d(i+1)} = \frac{-B_2 + \sqrt{B_2^2 - 4A_2C_2}}{2A_2}, \tag{2.2}$$

where $A_1 = (R_0-D)^2 - r^2$, $B_1 = 2L_{di}(R_0^2 - R_0D - r^2)$, $C_1 = (R_0^2 - r^2)L_{di}^2 - D^2r^2$, $A_2 = R_0^2 - r^2$, $B_2 = 2L_{si}(R_0^2 - R_0D - r^2)$, and $C_2 = [(R_0-D)^2 - r^2]L_{si}^2 - D^2r^2$.

III. RECONSTRUCTION ALGORITHM

III.A. Data transform from real detector to virtual detector

In the MBFEX system, the detector is not perpendicular to the central beams of the x-ray pixels $S_{\pm1}$. Therefore, the projections collected on the detector are not equal-spatial or equal-angular. For computation accuracy, the projections should be transformed from the real detectors to the virtual detectors, which are perpendicular to the center beams of the x-ray pixels. Let the object center be the coordinate origin, $S_i = (R_i \cos \lambda_i, R_i \sin \lambda_i)$ be each source position, P_r be any point on the real detector with coordinate u_r, P_v be any point on the virtual detector with coordinate u_v, D_{od} be the distance between the object center and the detector, D be the distance between the source S_0 and the detector, and $R_i, i \in \{0, \pm1\}$ be the source-to-virtual detector distances (see Fig. 3).
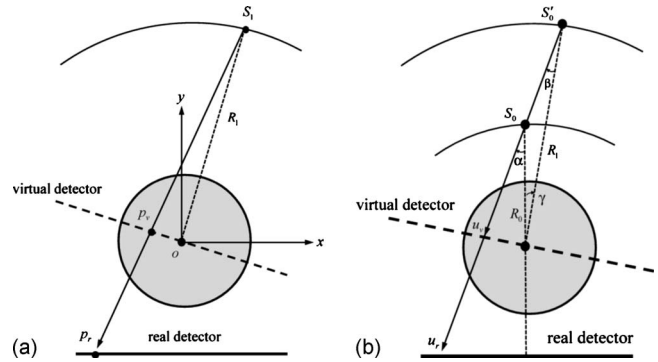
In Cartesian coordinates, $P_r = (x_r, y_r)$ and $P_v = (x_v, y_v)$ can be expressed as

$$\begin{cases} x_r = -u_r \\ y_r = -D_{od} \end{cases} \text{ and } \begin{cases} x_v = -u_v \sin \lambda_i \\ y_v = u_v \cos \lambda_i \end{cases}. \tag{3.1}$$

By the aforementioned construction we have

$$(P_r - S_i) = k(P_v - S_i), \tag{3.2}$$

where k is a real constant.

Substituting Eq. (3.1) into Eq. (3.2), it yields

$$\begin{cases} u_r + R_i \cos \lambda_i = k(u_v \sin \lambda_i + R_i \cos \lambda_i) \\ D_{od} + R_i \sin \lambda_i = k(-u_v \cos \lambda_i + R_i \sin \lambda_i) \end{cases}, \tag{3.3}$$

which implies

$$u_r = \frac{u_v \sin \lambda_i + R_i \cos \lambda_i}{-u_v \cos \lambda_i + R_i \sin \lambda_i}(R_i \sin \lambda_i + D_{od}) - R_i \cos \lambda_i. \tag{3.4}$$

Any beam irradiated from S_0 is equivalent to a beam started from the source S_0', which has a larger scanning radius R_1 [see Fig. 3(b)]. Let α and β be the angle between the beam and the central beam for S_0 and S_0', respectively. By construction,

$$\alpha = \tan^{-1}\frac{u_r}{D}, \quad \beta = \tan^{-1}\frac{u_v}{R_1}. \tag{3.5}$$

By the law of sines, we get

$$\frac{\sin(\pi - \alpha)}{R_1} = \frac{\sin \beta}{R_0}$$

and

$$\beta = \sin^{-1}\frac{R_0 \sin \alpha}{R_1}. \tag{3.6}$$

Substituting Eq. (3.6) into Eq. (3.5), we get the relationship between u_r and u_v. That is,

$$u_r = D \tan\left(\sin^{-1} \frac{R_1 \sin\left(\tan^{-1}\dfrac{u_v}{R_1}\right)}{R_0} \right), \quad \gamma = \beta - \alpha. \quad (3.7)$$

where γ determines the position of S_0'.

III.B. Reconstruction formula

The reconstruction formula for MBFEX system is derived from the conventional filtered backprojection algorithm.[12] It can be stated as follows:

$$\omega(\lambda, u) = \begin{cases} \sin^2\left(\dfrac{\pi}{4}\dfrac{\lambda}{\delta - \tan^{-1}(u/R)}\right), & 0 \le \lambda \le 2\delta - 2\tan^{-1}(u/R) \\ 1, & 2\delta - 2\tan^{-1}(u/R) \le \lambda \le \pi - 2\tan^{-1}(u/R) \\ \sin^2\left(\dfrac{\pi}{4}\dfrac{\pi + 2\delta - \lambda}{\delta + \tan^{-1}(u/R)}\right), & \pi - 2\tan^{-1}(u/R) \le \lambda \le \pi + 2\delta \end{cases}, \quad (3.10)$$

where $\lambda_e = \lambda_s + \pi + 2\delta$ and $\delta = \tan^{-1}(|u_{\max}|/R)$ is half the full fan angle of the central-scanning plane.

The images can be exactly reconstructed as long as the projections cover the angular range $\Delta = \pi + 2\sin^{-1}(r/R_1)$. Two cases are possible (see Fig. 4). For fixed r and R_1, if $R_0 \ge \sqrt{\frac{1}{2}(R_1^2 - rR_1)}$, Case A occurs. That is, the x-ray pixel S_1 moves from s_1 to s_1' across s_{-1} when the pixel S_{-1} moves from s_{-1} to s_{-1}'. Clearly, the trajectories of S_1 and S_{-1} cover the range Δ. Thus we could reconstruct the object without using the projections related to source S_0. If $R_0 < \sqrt{\frac{1}{2}(R_1^2 - rR_1)}$, Case B occurs. That is, the pixel S_1 moves from s_1 to s_1' when the source S_{-1} moves from s_{-1} to s_{-1}', and
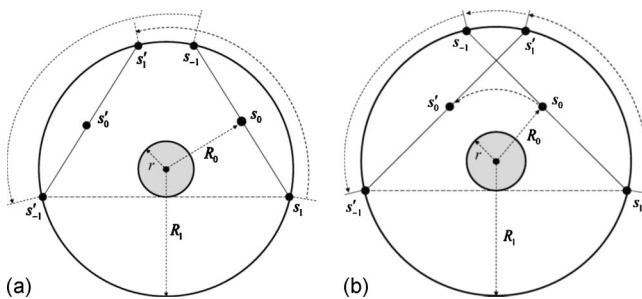

FIG. 4. Two possible cases when using half-scan algorithm. (a) Case A: The trajectories of S_1 and S_{-1} cover the minimum angle range; (b) Case B: The trajectories of S_0, S_1, and S_{-1} cover the minimum angle range.

$$f(x,y) = \frac{1}{2}\int_{\lambda_s}^{\lambda_e} \frac{R^2}{(R-s)^2} d\lambda \int_{-\infty}^{\infty} \omega(\lambda, u) g(\lambda, u)$$
$$\cdot h\left(\frac{Rt}{R-s} - u\right) \frac{R}{\sqrt{R^2 + u^2}} du, \quad (3.8)$$

where λ_s and λ_e are the starting and ending points of the backrprojection segment, h is the convolution kernel, $g(\lambda, u)$ is the projection specified by the angle λ of the scanning trajectory and the coordinate u on the detector, R is the scanning radius, and s and t are the rotated coordinate system defined as

$$\begin{bmatrix} s \\ t \end{bmatrix} = \begin{bmatrix} \cos\lambda & \sin\lambda \\ -\sin\lambda & \cos\lambda \end{bmatrix} \begin{bmatrix} x \\ y \end{bmatrix}. \quad (3.9)$$

The weight function ω is from Parker's half-scan weighting scheme.[13] Necessary changes have been made for the equal-spatial detector.

arc $\widehat{s_{-1}s_1'}$ are not covered by the trajectories of S_1 and S_{-1}. Notice that the pixel S_0 is also moving from s_0 to s_0' during the scanning. From the discussion in Sec. III A, the projections from pixel S_0 with radius R_0 can be transformed to those of a virtual source with radius R_1, and the trajectory of the virtual x-ray pixel covers the arc $\widehat{s_{-1}s_1'}$. Hence, the missing projections can be compensated by the transformed data over the arc $\widehat{s_{-1}s_1'}$.

IV. NUMERICAL EXPERIMENTS

To demonstrate the advantages of the proposed system and reconstruction scheme, we designed three numerical experiments with the well-known Shepp–Logan phantom. In the simulation, the MBFEX source had three x-ray pixels. The length of the detector was 300 mm for Case A and 550 mm for Case B. Each detector had 800 pixels per row. Given the object size $r = 35$ mm, the source to detector distance D, the x-ray pixel to x-ray pixel distance L_s, and the source to object distance R_0 can be calculated by Eq. (2.1). Then, we determined that if Case A (Case B) will occur by the condition discussed in Sec. III B. The parameters used in the simulations were listed in Table I. Actually, we should avoid the occurrence of Case B in practice because it may lead to a very large size of detector or the MBFEX source will be too

TABLE I. Parameters for numerical experiments.

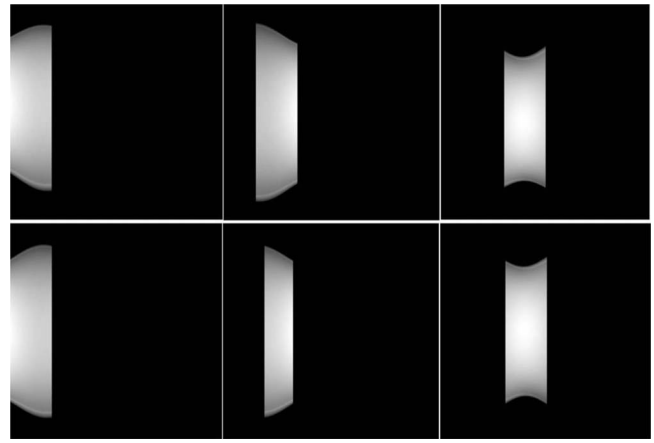|	Case A	Case B
D	800 mm	450 mm
R_0	600 mm	350 mm
L_s	292.5 mm	568.5 mm
L_d	300 mm	550 mm
r	35 mm	35 mm
Detector elements per row	800	800
Projections per round	800	800

FIG. 5. Projections on the real detectors and virtual detectors for Case B. From left to right, the columns are projections distributed on $[0, 0.385\pi]$, $[0.325\pi, 0.710\pi]$ ($[0.385\pi, 0.649\pi]$ after rebinning), and $[0.649\pi, 1.034\pi]$. They correspond to x-ray pixels S_1, S_0, and S_{-1}, respectively. The first row is for the projections collected on the real detectors, while the second row is for the rebinned projections on the virtual detectors. After rebinning in each image, the horizontal axis is for the views ranging from 0 to 2π and the vertical axis is for the detector bins.

close to the object. For all the simulations, we assumed that the x-ray pixels were identical (focal spot sizes, current, and kVp) to each other except for the locations.

In the first experiment, we used conventional half-scan algorithm to reconstruct the image, i.e., the data transform step discussed in Sec. III A is omitted. A reconstruction with our algorithm was also performed to verify the correctness of the proposed method. From Fig. 7, we observed that the reconstructed image was severely distorted, which indicated that x-ray source to detector element variations had great impact on the reconstruction. Fortunately, this issue can be readily fixed by employing a data rebinning process, as discussed in Sec. III A. After introducing the virtual detectors, different x-ray pixels can be seen as one x-ray source with different starting positions, so the reconstruction step can be treated as what we do for single source case.

In the second experiment, noise was considered when generating the projections. According to the Lambert–Beer law, the number of transmitted photons obeys the Poisson distribution and it is mainly determined by the number of photons emitted from the x-ray source to each detector cell. Setting the photon number N at different dose levels and following the steps described in Ref. 14, we obtained the projections associated with the Poisson noise, then reconstructed the image with our proposed algorithm. There was no observable difference in the simulation results between the MBFEX system and single source system at the same dose level (see Fig. 8).

The last experiment was to demonstrate that the MBFEX system is an effective way to reduce the scanning time, thus improving the image quality. We simulated a modified dynamic Shepp–Logan phantom, of which an eclipse centered at (7.7 mm, 0) rotated clockwise at 40° per round.

The algorithm was implemented as follows:

(1) Projection generation. Assuming that the phantom was centered at the origin, the MBFEX source and the detector were rotated simultaneously and continuously. The exposure time for each x-ray pixel is short enough to be ignored (compared to the detector readout time). 800 views were uniformly distributed over 2π for a complete cycle scanning. At each view, projections (or the line integral of the phantom density) were calculated by analytic method for every detector pixel (see the first

row of Fig. 5). In Fig. 5, the horizontal axis and the vertical axis in each image are for different views and detector bins, respectively.

(2) For pixels S_1 and S_{-1}, use Eq. (3.4) to transform the projections from the real detector to the virtual detector. For source S_0, use Eq. (3.7) to do the transformation. See the second row of Fig. 5.

(3) Compare the value of $\sqrt{\frac{1}{2}(R_1^2 - rR_1)}$ and R_0, then determine the required projections of each source; assume the starting angle of S_1 is 0. In Case A, the required data are $[0, 2\cos^{-1}(R_0/R_1)]$ for S_1 and $[2\cos^{-1}(R_0/R_1), \Delta]$ for S_{-1}. In Case B, the required data are $[0, \Delta - 2\cos^{-1}(R_0/R_1)]$, $[2\cos^{-1}(R_0/R_1), \Delta]$, and $[\Delta - 2\cos^{-1}(R_0/R_1), 2\cos^{-1}(R_0/R_1)]$ for pixels S_1, S_{-1}, and S_0, respectively.

(4) Combine the separated projections into one complete data set and apply the half-scan weighting function (3.10) (see Fig. 6). The projections are combined in se-
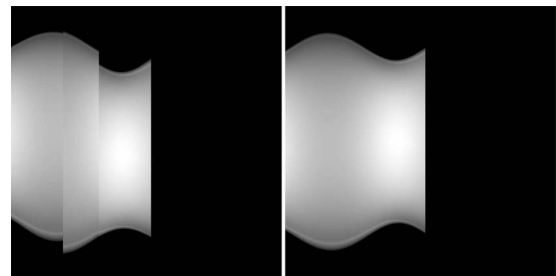

FIG. 6. Combined projections for half-scan reconstruction. Only 414 views were used in the reconstruction (153 views of S_1, 155 views of S_{-1}, and 106 views of S_0). Left: Combined projections without rebinning; right: Combined projections after rebinning.
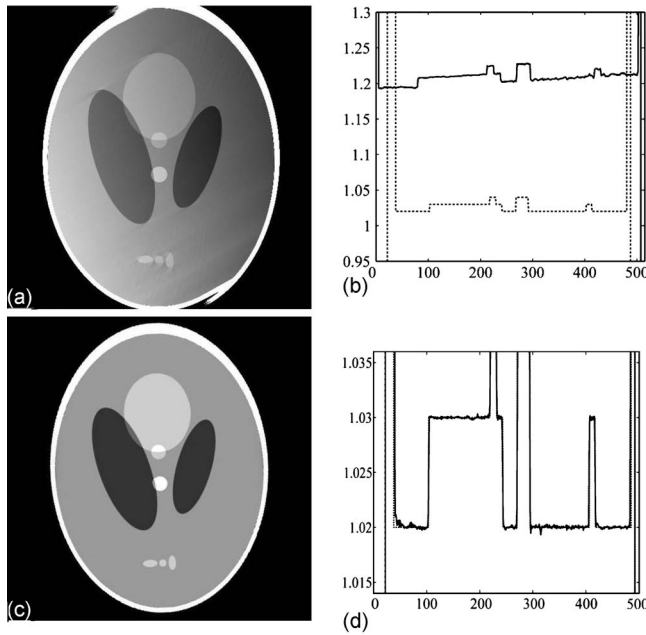
FIG. 7. Reconstructed images of the stationary Shepp–Logan phantom and their profiles. The projections were collected in the same MBFEX system for Case A, but the reconstruction algorithm for (a) was the conventional half-scan algorithm and for (c) was the proposed algorithm. (b) and (d) are profiles along $y=0$ and the dotted and solid lines are for the phantom and the reconstructed image, respectively. The display window is [0.99, 1.04].

quence, i.e., first S_1, then S_0 and S_{-1}. The edges are visible if the projections are combined without rebinning.

(5) Use Eq. (3.8) to reconstruct the object.

Simulation results are shown in Figs. 7–9. For comparison, in Fig. 9, images reconstructed by the conventional full-scan, half-scan algorithms from single source system are also displayed. All the images were obtained without any motion
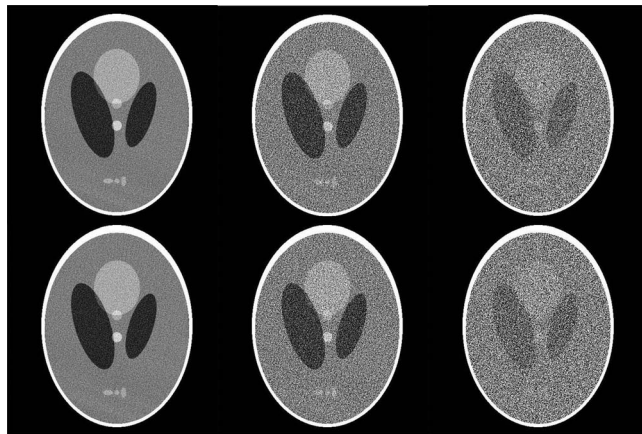

FIG. 8. Images reconstructed for a stationary Shepp–Logan phantom with different noise levels. Photon numbers N for left, middle, and right columns are 1.0×10^8, 1.0×10^7, and 1.0×10^6, respectively. The first row was reconstructed by the proposed algorithm for Case A, while the second row by the conventional half-scan algorithm for single source case. The display window is [0.99, 1.04].
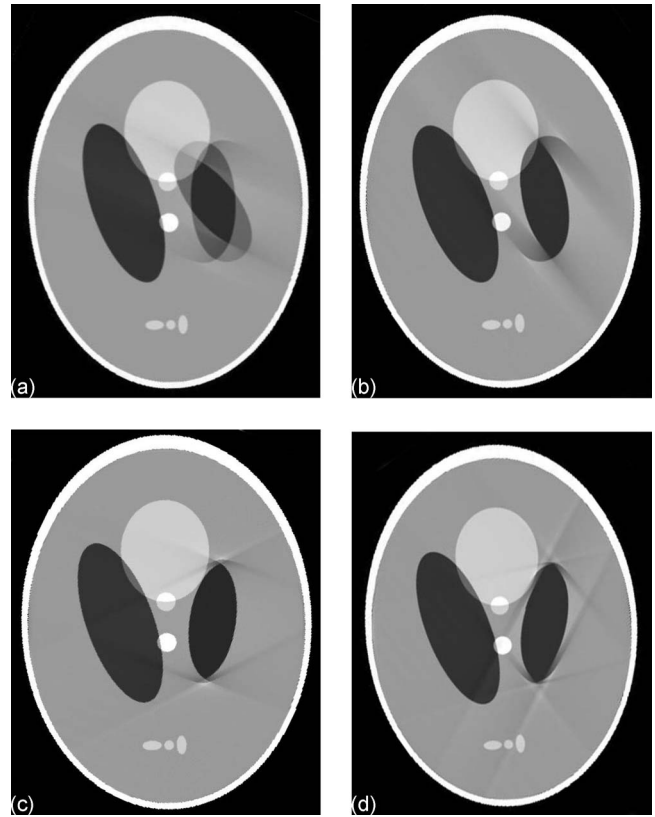
FIG. 9. Images reconstructed by (a) conventional full-scan algorithm; (b) conventional half-scan algorithm; (c) proposed half-scan algorithm with MBFEX system for Case A; and (d) proposed half-scan algorithms with MBFEX system for Case B. The display window is [0.99, 1.04].

correction process. Clearly, although the motion artifacts were still visible, they were significantly reduced with the optimized MBFEX system configuration.

V. DISCUSSION AND CONCLUSION

Compared to the single source geometry, the reduction of scanning time in the MBFEX system is not only determined by the algorithm we use but also affected by the ratio of L_s and R_0 (or the angle φ formed by pixels S_{-1}, S_1 and the center of the object). Let ρ be the scanning time reduction; then for the full-scan algorithm $\rho_f = \varphi/(2\pi)$ and for half-scan algorithm $\rho_h = \varphi/(\pi + 2 \sin^{-1}(r/R_1))$. Clearly, the larger φ is, the less scanning time will be, and the proposed MBFEX system associated with the half-scan algorithm can effectively reduce the scanning time.

Although the proposed algorithm has greatly reduced the redundant data, the data redundancy is still inevitable. For example, in Fig. 4(a), the data corresponding to the angular range $\widehat{s_{-1}s_1'}$ is obtained by both pixels S_{-1} and S_1, but only one of them is required for the algorithm. Recent research shows the utilization of the redundant data may help eliminating the artifacts and improving the noise uniformity,[15,16] thus yielding higher image quality. In the MBFEX system, a simple and effective way to fully utilize the redundant data is to give an equal weight to the overlapping projections, i.e., 1/2 to the data collected over the range $\widehat{s_{-1}s_1'}$ in Fig. 4(a). At
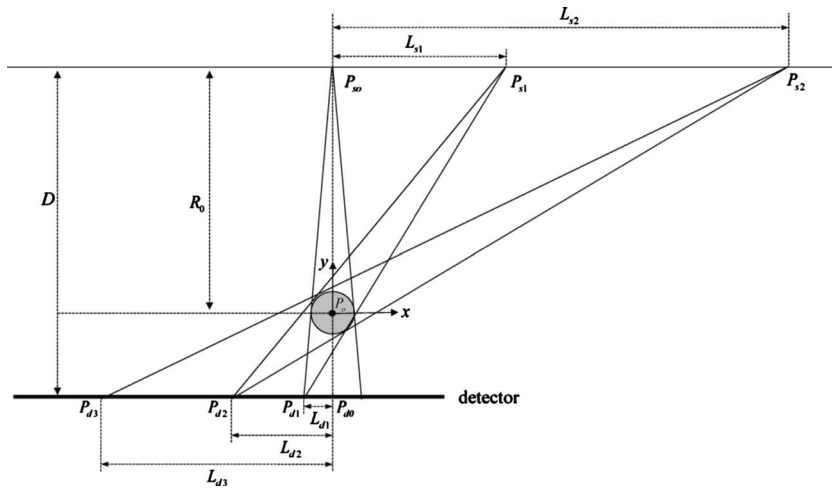
FIG. 10. The optimal design of the MBFEX system with N ($N \geq 3$) x-ray pixels.

the current stage, we are more interested in developing fan-beam algorithms for MBFEX system. However, the proposed algorithm could be readily extended to the 3D case in the well-known Feldkamp framework. For readers' interest, the cone-beam algorithm for MBFEX system is stated in Appendix B.

As indicated in Fig. 1, the MBFEX source array in our designs is linear in geometry. Understandably, a MBFEX source array in arc geometry or multisegment arrangement can provide better system geometry, which can result into more uniform geometry across different beams and potentially packing more beams with the same detector size. The reason that a linear MBFEX source instead of a curved source is used is the fabrication cost. The benefits from a curved MBFEX source are much more outweighed by the engineering costs. Alternatively, since MBFEX technology can tightly pack multiple x-ray pixels into a single linear x-ray tube, one might wonder why not simply use one such linear MBFEX tube tightly packed with dozens of x-ray pixels and turn on the desired x-ray beams for different designs. Our preliminary studies show the smallest pitch that two microfocused x-ray pixels can be packed together is ≥ 10 mm. With this constraint in mind, together with the limit on detector size, a linear MBFEX source array with dozens of x-ray pixels is not a good choice because it does not give fine enough freedom in adjusting the locations of x-ray pixels required in the design indicated in Fig. 1.

The MBFEX technique offers an opportunity for the innovation of multisource imaging system. The benefit of MBFEX system, such as its improved image quality for dynamic object, has been discussed in this paper. Other merits or shortcomings, i.e., its performances with compressive-sensing-based interior tomography, noise, and the dose/scattering reduction related issues will be studied in the future work.

ACKNOWLEDGMENTS

APPENDIX A: DERIVATION OF EQUATION (2.2)

First, let us consider the case when there are only three x-ray pixels. Denote the origin as $P_0 = (0,0)$, the center of the detector as $P_{d0} = (0, R_0 - D)$, and $P_{d2} = (-L_{d2}, R_0 - D)$, we have the equation of the line $P_{s1}P_{d2}$

$$y = \frac{D}{L_{s1} + L_{d2}}(x + L_{d2}) + R_0 - D \tag{A1}$$

and the distance r between the origin and line $P_{s1}P_{d2}$ is

$$r = \frac{\dfrac{DL_{d2}}{L_{s1} + L_{d2}} + R_0 - D}{\sqrt{\left(\dfrac{D}{L_{s1} + L_{d2}}\right)^2 + 1}}. \tag{A2}$$

Equation (A2) yields

$$R_0 = \frac{D \cdot L_s + r\sqrt{D^2 + \left(L_s + \frac{1}{2}L_d\right)^2}}{L_s + \frac{1}{2}L_d}, \tag{A3}$$

where the relationships $L_{d2} = \frac{1}{2}L_d$ and $L_{s1} = L_s$ have been used.

Second, let us consider the case when more sources are involved. Let $P_{si} = (L_{si}, R_0)$ be the source position, $P_{di} = (-L_{di}, R_0 - D)$, $P_{d(i+1)} = (-L_{d(i+1)}, R_0 - D)$, and $i = 1, 2 \ldots$ be the edge of the detector coverage of source S_i (see Fig. 10). Hence, we have the line $P_{si}P_{di}$

$$y = \frac{D}{L_{si} + L_{di}}(x + L_{di}) + R_0 - D \tag{A4}$$

and the line $P_{si}P_{d(i+1)}$

$$y = \frac{D}{L_{si} + L_{d(i+1)}}(x + L_{d(i+1)}) + R_0 - D. \tag{A5}$$

Since L_{di} is known and by the fact that the distance between P_0 and line $P_{si}P_{d(i+1)}$ is r, we can first calculate L_{si} by

$$L_{si} = \frac{-B_1 + \sqrt{B_1^2 - 4A_1C_1}}{2A_1}, \tag{A6}$$

where $A_1 = (R_0 - D)^2 - r^2$, $B_1 = 2L_{di}(R_0^2 - R_0D - r^2)$, and $C_1 = (R_0^2 - r^2)L_{di}^2 - D^2r^2$.

Then $L_{d(i+1)}$ can be computed by

$$L_{d(i+1)} = \frac{-B_2 + \sqrt{B_2^2 - 4A_2C_2}}{2A_2}, \tag{A7}$$

where $A_2 = R_0^2 - r^2$, $B_2 = 2L_{si}(R_0^2 - R_0D - r^2)$, and $C_2 = [(R_0 - D)^2 - r^2]L_{si}^2 - D^2r^2$.

APPENDIX B: CONE-BEAM ALGORITHM FOR MBFEX SYSTEM

Following the idea we derived from the fan-beam algorithm, before reconstruction, the projection data should be transformed from the real detector to a virtual detector. In 3D case, each projection collected on a two-dimensional detector array is denoted as (u, v). We have derived the data transform formulae in u-axes, so the remaining work is to locate the projection in v-axes.

In Fig. 3(a), the distance between S_1 and P_r can be computed as

$$S_1P_r = \sqrt{(R_1 \cos \lambda_1 + u_r)^2 + (R_1 \sin \lambda_1 + D_{od})^2} \tag{B1}$$

and the distance between S_1 and P_v is

$$S_1P_v = \sqrt{R_1^2 + u_v^2}. \tag{B2}$$

Since

$$\frac{v_v}{v_r} = \frac{S_1P_v}{S_1P_r}, \tag{B3}$$

substituting Eqs. (B1) and (B2) into Eq. (B3) gives

$$v_r = v_v \sqrt{\frac{(R_1 \cos \lambda_1 + u_r)^2 + (R_1 \sin \lambda_1 + D_{od})^2}{R_1^2 + u_v^2}}. \tag{B4}$$

The reconstruction formula for 3D case is derived from the general Feldkamp algorithm by Wang *et al.*[17] It can be described as follows:

$$f(x, y) = \frac{1}{2} \int_{\lambda_s}^{\lambda_e} \frac{R^2}{(R - s)^2} d\lambda \int_{-\infty}^{\infty} \omega(\lambda', u) g(\lambda, u, v)$$
$$\cdot h\left(\frac{Rt}{R - s} - u\right) \frac{R}{\sqrt{R^2 + u^2 + v^2}} du \tag{B5}$$

and the weight function are changed accordingly

$$\omega(\lambda', u) = \begin{cases} \sin^2\left(\frac{\pi}{4} \frac{\lambda'}{\delta' - \tan^{-1}(u/R')}\right), & 0 \le \lambda' \le 2\delta' - 2\tan^{-1}(u/R') \\ 1, & 2\delta' - 2\tan^{-1}(u/R') \le \lambda' \le \pi - 2\tan^{-1}(u/R') \\ \sin^2\left(\frac{\pi}{4} \frac{\pi + 2\delta' - \lambda'}{\delta' + \tan^{-1}(u/R')}\right), & \pi - 2\tan^{-1}(u/R') \le \lambda' \le \pi + 2\delta' \end{cases} \tag{B6}$$

where $\lambda' = \lambda/\sqrt{1 + v^2/R^2}$, $R' = \sqrt{R^2 + v^2}$, $\delta' = \tan^{-1}(|u_{max}|/R')$, $\lambda_e = \lambda_s + \pi + 2\delta$, and $\delta = \arctan(r/R)$ is half the full fan angle of the central-scanning plane.

a)Electronic mail: lvyang@sjtu.edu.cn

[1]C. Badea, L. Hedlund, and G. Johnson, "Micro-CT with respiratory and cardiac gating," Med. Phys. **31**, 3324–3329 (2004).

[2]G. Cao, Y. Z. Lee, R. Peng, Z. Liu, R. Rajaram, X. Calderon-Colon, L. An, P. Wang, T. Phan, S. Sultana, D. S. Lalush, J. P. Lu, and O. Zhou, "A dynamic micro-CT scanner based on a carbon nanotube field emission x-ray source," Phys. Med. Biol. **54**, 2323–2340 (2009).

[3]G. Cao, X. Calderon-Colon, P. Wang, L. Burk, Y. Lee, R. Rajaram, S. Sultana, D. Lalush, J. Lu, and O. Zhou, "A dynamic micro-CT scanner with a stationary mouse bed using a compact carbon nanotube field emission x-ray tube," Proc. SPIE **7258**, 72585Q–1 (2009).

[4]C. T. Badea, B. Fubara, L. W. Hedlund, and G. A. Johnson, "4-D micro-CT of the mouse heart," Mol. Imaging **4**, 110–116 (2005).

[5]R. A. Robb, E. A. Hoffman, L. J. Sinak, L. D. Harris, and E. L. Ritman, "High-speed three-dimensional x-ray computed tomography: The dynamic spatial reconstructor," Proc. IEEE **71**, 308–319 (1983).

[6]J. Zhang, G. Yang, Y. Cheng, B. Gao, Q. Qiu, Y. Lee, J. Lu, and O. Zhou, "Stationary scanning x-ray source based on carbon nanotube field emitters," Appl. Phys. Lett. **86**, 184104 (2005).

[7]X. Qian, R. Rajaram, X. Calderon-Colon, G. Yang, T. Phan, D. Lalush, J. Lu, and O. Zhou, "Design and characterization of a spatially distributed multibeam field emission x-ray source for stationary digital breast tomosynthesis," Med. Phys. **36**, 4389–4399 (2009).

[8]J. Maltz, F. Sprenger, J. Fuerst, A. Paidi, F. Fadler, and A. Bani-Hashemi, "Fixed gantry tomosynthesis system for radiation therapy image guidance based on a multiple source x-ray tube with carbon nanotube cathodes," Med. Phys. **36**, 1624–1636 (2009).

[9]T. Zhang, D. Schulze, X. Xu, and J. Kim, "Tetrahedron beam computed tomography (TBCT): A new design of volumetric CT system," Phys. Med. Biol. **54**, 3365–3378 (2009).

[10]R. Peng, J. Zhang, X. Calderon-Colon, S. Wang, S. Sultana, S. Chang, J. Lu, and O. Zhou, "Stationary micro-CT scanner using a distributed multibeam field emission x-ray source: A feasibility study," Proc. SPIE **7258**, 725847 (2009).

[11]E. Quan and D. Lalush, "A faster OSC algorithm for iterative reconstruction in a rotation-free micro-CT system," Phys. Med. Biol. **54**, 1061–1072 (2009).

[12]A. Kak and M. Slaney, *Principles of Computerized Tomographic Imaging* (IEEE Press, New York, 1999).

[13]D. Parker, "Optimal short scan convolution reconstruction for fan beam CT," Med. Phys. **9**, 254–257 (1982).

[14]H. Yu, Y. Ye, S. Zhao, and G. Wang, "Local ROI reconstruction via generalized FBP and BPF algorithms along more flexible curves," Int. J. Biomed. Imaging **2006**, 1–7 (2006).

[15]S. Mori, M. Endo, T. Obata, R. Kishimoto, H. Kato, S. Kandatsu, H. Tsujii, and S. Tanada, "Noise properties for three weighted Feldkamp algorithms using a 256-detecotor row CT-scanner: Case study for hepatic volumetric cine imaging," Eur. J. Radiol. **59**, 289–294 (2006).

[16]D. Heuscher, K. Brown, and F. Noo, "Redundant data and exact helical cone-beam reconstruction," Phys. Med. Biol. **49**, 2219–2238 (2004).

[17]G. Wang, T. Lin, P. Cheng, and D. Shinozaki, "A general cone-beam reconstruction algorithm," IEEE Trans. Med. Imaging **12**, 486–496 (1993).